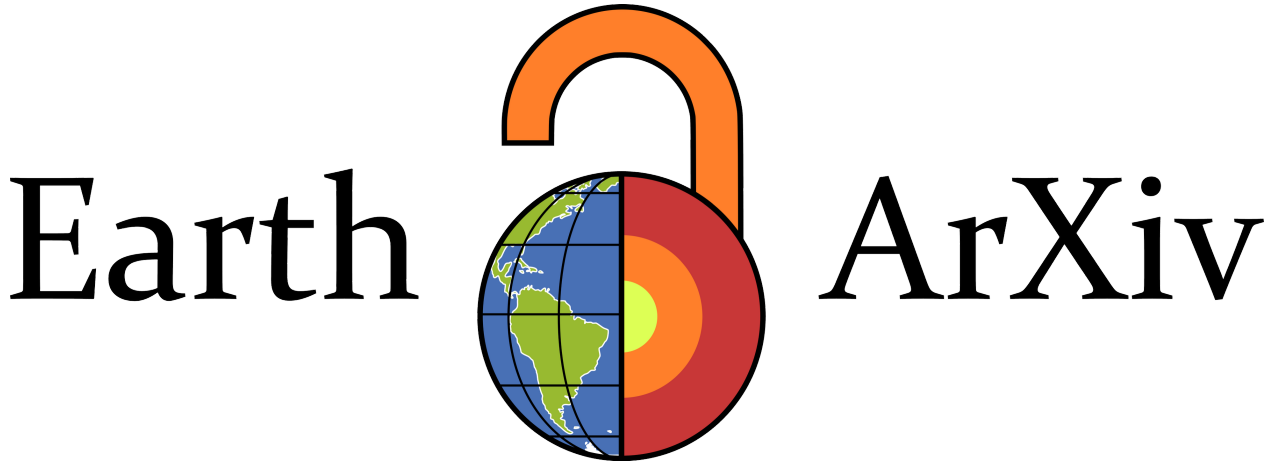

Rapid SRO aluminosilicate formation in a narrow pH interval fractionates silicon isotopes

K. Russo[1], H.T. Jamison[1,2], L.A. Derry[1], N.M. Fernandez[1,2*]

[1]Department of Earth and Atmospheric Sciences, Cornell University, Ithaca, New York, USA

[2]Department of Earth and Planetary Sciences, ETH Zürich, Zürich, Switzerland

*Corresponding author:

Nicole M. Fernandez (nicole.fernandez@eaps.ethz.ch)

Rapid SRO aluminosilicate formation in a narrow pH interval fractionates silicon isotopes

K. Russo[1], H.T. Jamison[1,2], L.A. Derry[1], N.M. Fernandez [1,2*]

[1]Department of Earth and Atmospheric Sciences, Cornell University, Ithaca, New York, USA

[2]Department of Earth and Planetary Sciences, ETH Zürich, Zürich, Switzerland

*Corresponding author: Nicole M. Fernandez (nicole.fernandez@eaps.ethz.ch)

Abstract

Short-range ordered (SRO) hydrous aluminosilicates (HAS) are among the earliest secondary phases formed during incongruent silicate weathering, yet the timescales and silicon isotope ($\delta^{30}Si$) fractionation associated with their initial formation remains poorly constrained. We use stepwise room temperature NaOH titration to resolve pH buffering, Si–Al removal, and dissolved $\delta^{30}Si$ evolution in two complementary organosilicate-derived Si experiments and an experiment with an inorganic silica source. All three titrations (initial Si/Al ≈ 1) showed coupled Si–Al removal across a narrow pH interval and converged on Al-rich net uptake in solid phases (Si/Al ≈ 0.47 – 0.52). FTIR, XRD, and SEM of recovered precipitates support poorly ordered allophanic SRO HAS products. In the organosilicate-derived experiments, dissolved $\delta^{30}Si$ increased by ~ 2 ‰ as Al was removed. First-order Rayleigh models yield apparent kinetic isotope fractionation factors of – 2.56 to -2.08 ‰, although late-stage deviations show that no single factor captures the full trajectory. These results identify allophane-like SRO HAS formation as a rapid process for generating measurable $\delta^{30}Si$ signatures during incipient weathering.

Introduction

The neoformation of secondary clay minerals during chemical weathering is a fundamental control on soil architecture, solute retention, and major (bio)geochemical pathways in the Critical Zone (Schroeder, 2018a, 2018b). Among the earliest secondary phases formed when silicon (Si) and aluminium (Al) are released during primary silicate dissolution are poorly crystalline, short-range ordered (SRO) hydrous aluminosilicates (HAS), including allophane-like phases ($Al_2O_3(SiO_2)_{1.3-2}\cdot[2.5\text{-}3]H_2O$) (Harsh, 2005). These phases are common in volcanic weathering sequences (Levard *et al.*, 2012; Wada, 1978), but also occur across a broader range of temperature, montane, and sedimentary weathering environments (Gustafsson *et al.*, 1998; Harsh, 2005; Nelson *et al.*, 2021; Parfitt, 2009). Allophane-like SRO HAS are highly reactive and metastable and, thus, can act as precursor phases during the progression from primary mineral dissolution towards more crystalline clay assemblages (Harsh, 2005; Lenhardt *et al.*, 2021; Parfitt, 2009). Their formation is therefore important not only for understanding clay mineral evolution, but also for interpreting the geochemical and isotopic signatures generated during incipient, incongruent weathering.

Experimental studies have shown that SRO HAS formation is controlled by pH, aqueous Si/Al, and the availability of hydrolysed Al species. Classic synthesis experiments required heating to 95 - 100 ˚C over several days (Wada *et al.*, 1979), whereas subsequent work demonstrated room temperature formation via condensation of silicic acid onto hydroxy-aluminosilicate templates (Doucet *et al.*, 2001). Further work showed SRO HAS formation was favoured under acidic to near-neutral (pH ~ 3 - 6) conditions, with pH and Al/Si dictating the stoichiometry and solubility (Baldermann *et al.*, 2024). Together, these studies establish that the onset and composition of SRO HAS precipitation is governed by coupled pH and Al–Si speciation.

Silicon stable isotopes ($\delta^{30}Si$) provide a complementary way to trace this transfer of Si from primary minerals into secondary phases and dissolved weathering products (Frings *et al.*, 2021; Opfergelt and Delmelle, 2012). Field and experimental studies have shown that secondary mineral formation preferentially removes light ^{28}Si isotopes from solution, leaving residual fluids enriched in the heavy ^{30}Si relative to the dissolving parent bedrock (Basile-Doelsch, 2006). In basaltic weathering systems, this process contributes to progressively lighter $\delta^{30}Si$ in weathered soils as increasing fractions of Si are retained in neoformed secondary minerals, whereas soil and river waters carry comparatively heavier dissolved $\delta^{30}Si$ signatures (Opfergelt *et al.*, 2012; Ziegler *et al.*, 2005). Ziegler *et al.* (2005) provided a key first experimental constraint on this process by showing that allophane preferentially incorporates isotopically light ^{28}Si. However, the timescales, geochemical controls, and apparent magnitude of $\delta^{30}Si$ fractionation during the onset of SRO HAS precipitation remains poorly constrained.

Here we use stepwise NaOH titration at room temperature to resolve the onset and progression of allophane-like SRO HAS formation across a narrow pH interval. By tracking pH, dissolved Si and Al, and fluid $\delta^{30}Si$ through the pH-buffering and post-removal stages, we directly link Si isotope evolution to reaction progress. These results provide a process-level experimental constraint on how early-stage aluminosilicate formation can generate measurable Si isotope fractionation.

Materials and Methods

Three room temperature (~20 ºC) NaOH titration experiments were conducted across two dissolved Si source pathways, which we term "organosilicate-derived" and "SiO_2-derived". Organosilicate-derived experiments A and B used filtered, preconditioned residual fluids from the same 30 ºC Si–Al precursor pathway, prepared by TEOS (tetraethyl orthosilicate) hydrolysis followed by Al addition (Wada *et al.*, 1979). Further Si–Al removal in the precursor fluids had slowed under persistently acidic conditions near pH 3.8. Experiment A used fluid collected after 28 days of preconditioning and began at 3.24 mM molybdate-reactive Si (henceforth referred to as "dissolved Si"), 3.59 mM Al (Si/Al = 0.90), and fluid $\delta^{30}Si$ = -2.64 ± 0.08 ‰. All reaction progress quantities (f_{Si}, f_{Al}, $(Si/Al)_{removed}$) and Rayleigh models are defined on molybdate-reactive Si, which tracks the monomeric and small oligomeric pool available for reaction (Iler, 1979). Experiment B used fluid collected after 14 days and began at 3.25 mM dissolved Si, 3.25 mM Al

(Si/Al = 1.00), and $\delta^{30}Si$ = -2.45 ± 0.15 ‰. These experiments are treated as complementary configurations instead of strict replicates. The SiO_2-derived experiment used a mixed solution prepared from an inorganic Si source obtained by dissolving amorphous SiO_2 seeds, and $AlCl_3$, with initial concentrations of 1.28 mM dissolved Si, 1.26 mM Al (Si/Al = 1.02), and fluid $\delta^{30}Si$ = -1.77 ± 0.05 ‰. Total dissolved Si (ICP-OES) were measured for the SiO_2-derived titration and exceeded reactive Si by up to ~ 0.4 mM (Table S-2). Minor silica polymerisation cannot be fully excluded in the mildly supersaturated organosilicate-derived fluids (Fig. S-1d; Supplementary Information).

To resolved pH buffering and associated Si–Al removal, 0.1 M NaOH was added stepwise across pH ~ 4 – 8, with post-addition mixing. Experiment A and the SiO_2-derived experiment used independent 15 mL aliquots sampled after 24 hours. Experiment B was titrated continuously in a 250 mL reactor and sampled after pH stabilisation, typically within 3 – 5 minutes. Samples were filtered at 0.22 µm before measurement of dissolved Si, dissolved Al, and Si isotope composition. Precipitates were washed, dried and characterized by X-Ray Diffraction (XRD), Fourier Transform Infrared (FTIR) Spectroscopy and Scanning Electron Microscopy (SEM). Full preparation, experimental details, analytical procedures and datasets are provided in the Supplementary Information.

Results and Discussion

A narrow pH-buffering window marks the onset of Si–Al removal. Stepwise NaOH addition produced a distinct pH-buffering interval between pH ~ 4 – 5 in all three experiments (**Fig. 1**). In organosilicate-derived experiment A, the principal removal interval occurred between pH 4.25 and 4.88, across which dissolved Si decreased from 3.09 to 1.50 mM and dissolved Al decreased from 3.46 to 0.25 mM (**Fig. 2a,b**). Experiment B reproduced this response between pH 4.04 and 4.72, with dissolved Si decreasing from 3.25 to 2.08 mM and dissolved Al from 3.06 to 0.51 mM. Al removal continued between the final two B samples and reached below detection at pH 6.03, while Si decreased further to a final concentration of 1.67 mM. The independently prepared SiO_2-derived experiment showed the same coupled response between pH 4.29 and 4.79, with dissolved Si decreasing from 1.24 to 0.72 mM and Al from 1.20 to 0.06 mM. Coupled removal during pH buffering is consistent with alkalinity-driven Al hydrolysis and Si–Al condensation during SRO HAS formation (Lenhardt *et al.*, 2021).

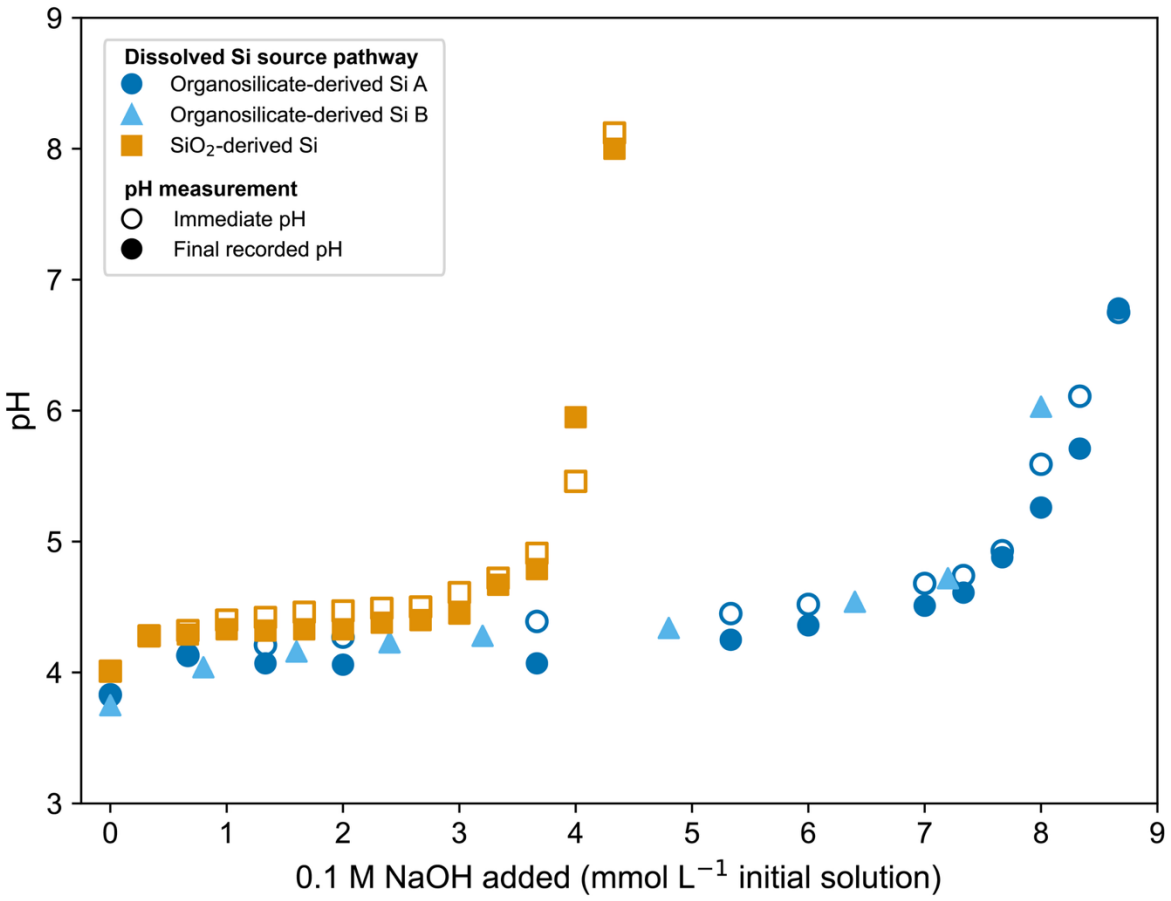

Figure 1. Evolution of pH during stepwise NaOH titration of mixed Si–Al starting solutions. Open symbols show the pH measured immediately after each NaOH volumetric addition, and filled symbols show stabilised pH. Experiment B was sampled after pH stabilisation without immediate post-addition readings (Table S-1).

Allophane-like SRO HAS formed at room temperature. The aqueous and solid-phase data together support formation of allophanic SRO HAS at room temperature. All experiments exhibited coupled Si–Al removal across the pH-buffered interval, consistent with the precipitation of an Al-bearing silicate phase. To constrain the stoichiometry of net solute removal, we calculated the cumulative $(Si/Al)_{removed}$ ratio from aqueous mass balance (**Eq. 1**):

$$\left(\frac{Si}{Al}\right)_{removed} = \frac{[Si]_0 - [Si]_n}{[Al]_0 - [Al]_n} \quad \text{(Eq. 1)}$$

where $[Si]_0$ and $[Al]_0$ correspond to the initial dissolved silicon and aluminium concentration respectively. $[Si]_n$ and $[Al]_n$ represent the respective dissolved concentrations at each discrete sample interval. This ratio provides an operational estimate of the integrated Si/Al stoichiometry of Si and Al removed from solution and, where a single phase dominates uptake, approximates the composition of the solid precipitates. Because early titration steps are sensitive to the analytical scatter, we interpret it over the interval of substantial Si–Al loss. Despite initial Si/Al of 0.9 – 1.02, all three experiments ultimately converged on similarly Al-rich net uptake with $(Si/Al)_{removed}$ =

0.47 to 0.52 (**Fig. 2c**), within or close to compositions reported for synthetic allophanic SRO HAS (Baldermann *et al.*, 2024; Doucet *et al.*, 2001; Ohashi *et al.*, 2002; Wang *et al.*, 2018).

Solid-phase characterisation was performed on precipitates recovered from organosilicate-derived A and SiO_2-derived experiments. Together, FTIR, XRD, and SEM provide complementary evidence for formation of an allophanic SRO HAS-dominated product (**Fig. 3**). FTIR spectra contain the broad OH/H_2O, Si–O, Al –O– Si, and O–Si–O vibrational envelopes expected for SRO aluminosilicates (**Fig. 3a,** Baldermann *et al.*, 2018; Levard *et al.*, 2012). XRD patterns are characterized by broad features and lack sharp reflections diagnostic of crystalline aluminosilicates (**Fig. 3b**). SEM images show aggregated, rounded nanoparticulate clusters (**Fig. 3c-e**), a commonly observed morphological tendency of SRO HAS phases (Lenhardt *et al.*, 2021). Allophane, proto-imogolite, and related imogolite-type materials can share similar local Si–Al environments (Du *et al.*, 2022; Levard *et al.*, 2012). We therefore describe the products as allophanic SRO HAS rather than a structurally mature allophane (Lenhardt *et al.*, 2021).

Saturation-index calculations provide a thermodynamic consistency test for this interpretation (Supplementary Information, Baldermann *et al.*, 2024). Across the active removal intervals (pH ~ 4 – 5), the solutions were strongly oversaturated with respect to their experiment-specific SRO HAS phases, with SI_{HAS} ranging from +3.27 to +4.46 in experiment A, +1.80 to +4.07 in experiment B, and +2.27 to +2.77 in the SiO_2-derived experiment (Fig. S-1a). All three remained undersaturated with respect to amorphous $Al(OH)_3$ over the same intervals (Fig. S-1b). Although gibbsite was nominally supersaturated (Fig. S-1c), this does not establish its precipitation over the experimental timescales (Nagy and Lasaga, 1993). The calculations therefore support a strong thermodynamic driving force for SRO HAS formation and argue against amorphous $Al(OH)_3$ as a major independent sink during rapid Al removal.

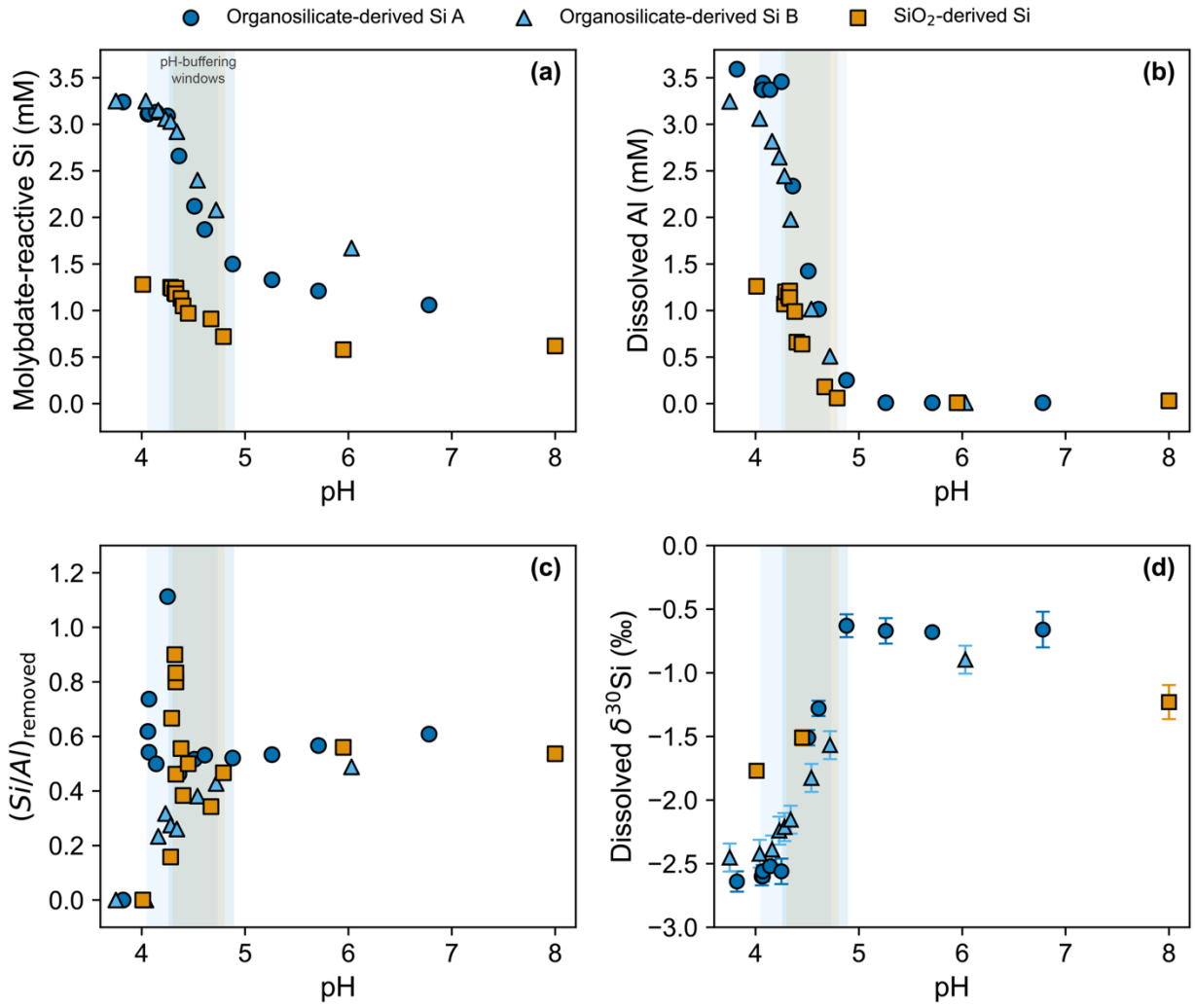

Figure 2. pH-dependent Si-Al removal and Si stable isotope evolution. **(a)** Molybdate-reactive Si, **(b)** dissolved Al, **(c)** cumulative $(Si/Al)_{removed}$, and **(d)** dissolved $\delta^{30}Si$ plotted against stabilised pH for all three experiments. Error bars in **(d)** represent 2σ analytical uncertainty. Shaded areas designate experiment-specific pH-buffering windows (adopting same colour scheme).

Dissolved $\delta^{30}Si$ tracks pH-driven Si removal. Dissolved $\delta^{30}Si$ increased over the same reaction interval in which Si and Al were removed from solution (**Fig. 2**). In organosilicate-derived experiment A, $\delta^{30}Si$ remained near its initial value during the early titration steps, when dissolved Si and Al changed only modestly. The principal $\delta^{30}Si$ shift occurred between pH 4.25 and 4.88, where dissolved $\delta^{30}Si$ increased from -2.56 ± 0.10 ‰ to -0.63 ± 0.09 ‰ as f_{Si} decreased from 0.95 to 0.46. Experiment B reproduced this pattern over the shorter pH-stabilisation intervals. Dissolved $\delta^{30}Si$ increased from an initial -2.45 ± 0.15 ‰ to -1.57 ± 0.11 ‰ at pH 4.72 and reached -0.90 ± 0.09 ‰ at pH 6.03 as dissolved Al fell below detection. Together, the two organosilicate-derived experiments show that the main isotope shift developed during progressive Al-coupled Si removal.

The SiO_2-derived experiment shows the same direction of $\delta^{30}Si$ evolution. Dissolved $\delta^{30}Si$ increased from an initial -1.77 ± 0.05 ‰ to -1.51 ± 0.06 ‰ within the removal interval, reaching -1.23 ± 0.13 ‰ in the final sample at pH 8.0 that extends outside the active Si–Al removal period. This gradual enrichment of the residual fluids in the heavy ^{30}Si isotope across both Si source pathways is consistent with preferential incorporation of the light ^{28}Si into the newly formed SRO HAS precipitates (Oelze *et al.*, 2015; Ziegler *et al.*, 2005). We therefore use Rayleigh models below as first-order predictions of the apparent net kinetic isotope effects expressed in the early stages of mineral growth (Fernandez *et al.*, 2019; Oelze *et al.*, 2015; Roerdink *et al.*, 2015).

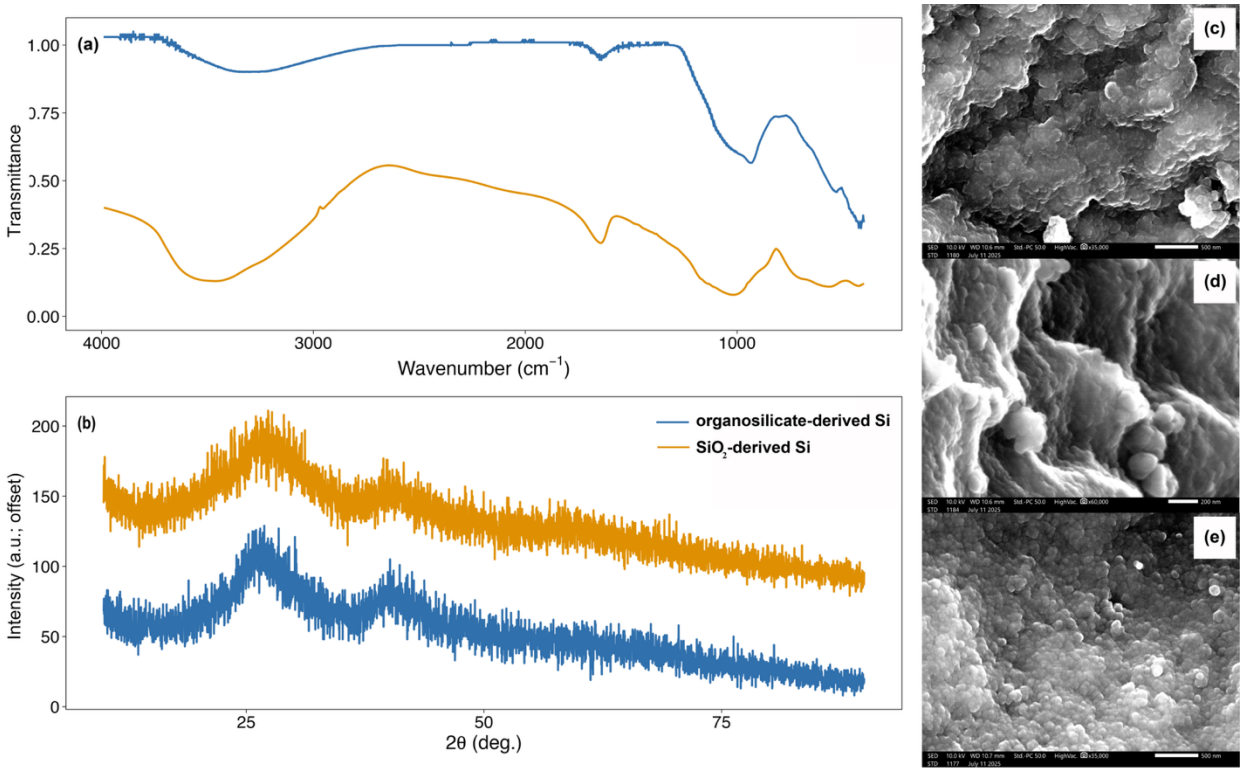

Figure 3. Solid-phase characterisation of precipitates recovered from the organosilicate-derived Si experiment B and SiO_2-derived titrations. **(a)** FTIR spectra normalized and offset for clarity-comparisons are based on broad adsorption envelopes rather than absolute intensities or exact peak positions. **(b)** XRD patterns showing broad features consistent with short-range structural order. Patterns are also offset vertically for clarity. SEM images show aggregated nanoparticulate material in the organosilicate-derived precipitate at **(c)** lower and **(d)** higher magnification and **(e)** SiO_2-derived precipitate. Scale bars are 500 nm in (c and e) and 200 nm in (d).

Rayleigh-derived apparent fractionation factors differ between Si starting solution pathways. Dissolved $\delta^{30}Si$ covaried closely with the fraction of Al remaining in solution (f_{Al}) in both organosilicate-derived experiments (**Fig. 4a**), linking stable isotope evolution to coupled Si–Al removal. We used Rayleigh models (Frings *et al.*, 2016; Rayleigh, 1902) as first-order descriptions

of the net isotope effect recorded during progressive Si removal (**Fig. 4b**, Eqs. S-5, S-7). In experiment A, the full trajectory yields an apparent fractionation factor ($\varepsilon \approx 1000 \times ln\alpha$, Eq. S-6) of -2.08 ± 0.03 ‰, whereas restricting the model to only the Al-coupled Si removal interval yields a larger ε of -2.56 ± 0.07 ‰. Experiment B independently records an apparent ε of -2.20 ± 0.13 ‰ over the shorter pH-stabilisation timescale.

A single constant- ε trajectory does not describe the complete organosilicate-derived experiment A dataset. Once dissolved Al fell below detection, Si continued to decrease from 1.33 to 1.06 mM while dissolved δ^{30}Si stabilized near -0.67 ‰. This late-stage divergence indicates that the kinetic isotopic effect was expressed primarily during Al-coupled precipitation. Subsequent Si removal may reflect silica polymerisation, sorption, or partial re-equilibration (Lenhardt *et al.*, 2021; Oelze *et al.*, 2015), none of which is distinguished by the present data. Experimental and modelling studies show that apparent Si isotope fractionation can depend on net precipitation rate and can also continue to exchange as back-reaction or surface exchange becomes important (Fernandez *et al.*, 2019; Oelze *et al.*, 2015; Roerdink *et al.*, 2015).

A descriptive Rayleigh fit through the three SiO_2-derived dissolved δ^{30}Si measurements yields an apparent ε of -0.80 ± 0.14 ‰ (Table S-3). Given the limited data (n = 3), we treat this value as descriptive rather than a robust pathway-specific fractionation factor. The measured precipitate δ^{30}Si of -2.19 ± 0.11 ‰ nevertheless falls close to the accumulated product predicted by the Rayleigh curve (**Fig. 4b**), providing independent mass-balance support for preferential ^{28}Si incorporation into the solid phase product.

The organosilicate-derived apparent ε values are comparable to the allophane synthesis experiments of Ziegler *et al.* (2005), which used the same TEOS-derived silica chemistry but were conducted at 95 ºC without time-resolved sampling (ε ≈ -1.8 ‰). The agreement extends to the ~2 ‰ solid solution δ^{30}Si offset they documented across the Hawaiian chronosequence, suggesting that the fractionation expressed during rapid SRO HAS formation at room temperature is comparable in magnitude to that recorded in natural weathering systems. The SiO_2-derived trajectory shares the same direction but a smaller apparent magnitude. In previous experiments, measurable δ^{30}Si fractionation occurred primarily in the presence of an Al-bearing carrier phase and increased with net-solid formation, from near zero to -5 ‰, whereas pure silicic acid polymerisation produced little fractionation (Oelze *et al.*, 2015). The expressed isotope effect may reflect rate-dependent adsorption or incorporation at reactive Al-bearing surfaces (Oelze *et al.*, 2015), followed by surface exchange or back-reaction that permits partial isotopic re-equilibration (DePaolo, 2011; Fernandez *et al.*, 2019). These processes may be mechanistically linked because the same newly formed surfaces that initially remove Si can subsequently mediate isotope exchange. We therefore interpret the contrasting apparent ε values as pathway-specific net isotope effects integrating initial Si uptake and subsequent exchange rather than intrinsic fractionation

factors specific to SRO HAS. Differences in Si source, concentration, preconditioning history, and experimental configuration preclude attributing the contrast to precipitation rate alone.

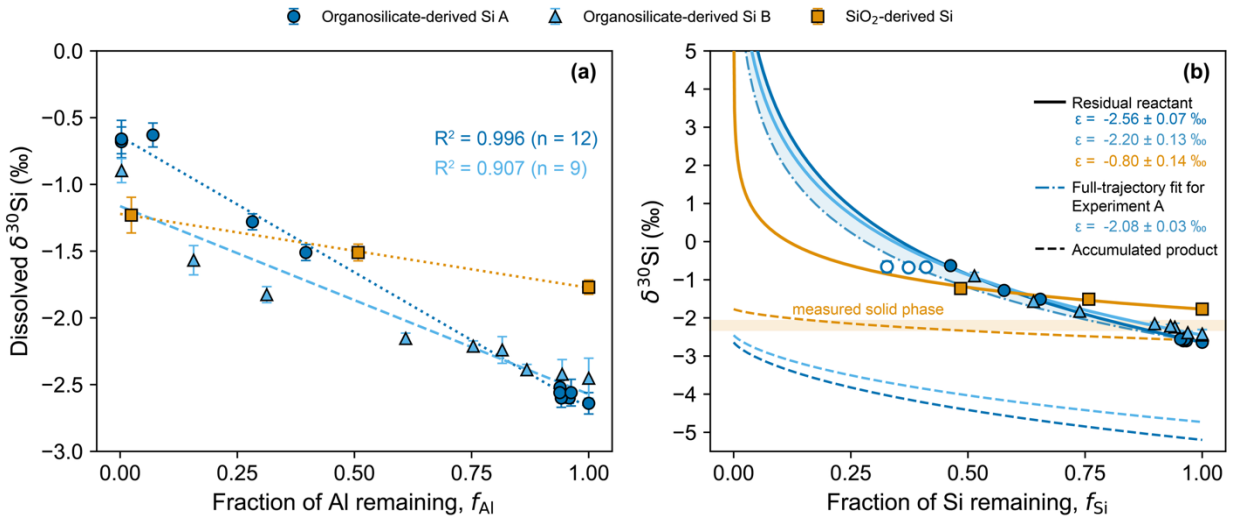

Figure 4. Si isotope evolution during SRO HAS formation. **(a)** Dissolved δ^{30}Si versus fraction of Al remaining in solution (f_{Al}). Reduced major axis (RMA) regressions are shown for all three experiments (Supplementary Information). **(b)** First-order Rayleigh model predictions of dissolved δ^{30}Si versus the fraction of Si remaining (f_{Si}). Curves show the Al-coupled and full-trajectory fits for experiment A, the experiment B fit and the descriptive SiO_2-derived trajectory. Dashed curves represent the calculated accumulated products (Eq. S-7), and the shaded yellow area shows the measured precipitate from the inorganic silica (SiO_2)-derived experiment. Error bars correspond to 2σ and in **(b)** are smaller than the symbols.

Conclusions

Stepwise NaOH titrations resolved the rapid transition from metastable acidic Si–Al fluids to allophanic SRO HAS precipitation. Across three complementary experiments (Si/Al ~ 1), coupled Si–Al removal occurred largely within a narrow pH-buffering interval and generated measurable apparent δ^{30}Si fractionation over rapid (minutes to hours) timescales. The two organosilicate-derived experiments provide reproducible quantitative trajectories, whereas the independently prepared SiO_2-derived experiment confirms the direction of fractionation and corresponding accumulation of an isotopically light ^{28}Si solid product. These results support field interpretations in which isotopically light secondary phases drive heavier dissolved δ^{30}Si during desilication (Opfergelt *et al.*, 2012) and along reactive flow paths (Guertin *et al.*, 2024). Rayleigh models provide useful first-order apparent descriptions but do not capture the complete post-Al depletion stabilisation. Our findings demonstrate SRO HAS formation can imprint dissolved δ^{30}Si over experimental timescales of minutes to 24 hours, providing a mechanistic basis for interpreting Si isotope signatures generated during incipient incongruent weathering and refining the interpretation of Si stable isotopes in the Critical Zone (Frings *et al.*, 2021).

Acknowledgements

This work was supported by the President's Council of Cornell Women (PCCW) Affinito-Stewart Grant and US National Science Foundation EAR-2308547. K.R. received support by the National Science Foundation Graduate Fellowship Program under Grant No. DGE – 2139899 and Cornell University's Colman Fellowship.

References

Baldermann, A., Grießbacher, A.C., Baldermann, C., Purgstaller, B., Letofsky-Papst, I., Kaufhold, S., Dietzel, M. (2018) Removal of Barium, Cobalt, Strontium, and Zinc from Solution by Natural and Synthetic Allophane Adsorbents. *Geosciences*. Multidisciplinary Digital Publishing Institute 8, 309.

Baldermann, A., Stamm, F.M., Farkaš, J., Löhr, S., Ratz, B., Letofsky-Papst, I., Dietzel, M. (2024) Precipitation of short-range order hydroxy aluminosilicate (HAS) and hydrous ferric silicate (HFS) at ambient temperature: Insights into mineral formation pathways, crystal chemistry and solubility-stability relationships. *Chemical Geology* 646, 121911.

Basile-Doelsch, I. (2006) Si stable isotopes in the Earth's surface: A review. *Journal of Geochemical Exploration* 88, 252–256.

DePaolo, D.J. (2011) Surface kinetic model for isotopic and trace element fractionation during precipitation of calcite from aqueous solutions. *Geochimica et Cosmochimica Acta* 75, 1039–1056.

Doucet, F.J., Schneider, C., Bones, S.J., Kretchmer, A., Moss, I., Tekely, P., Exley, C. (2001) The formation of hydroxyaluminosilicates of geochemical and biological significance. *Geochimica et Cosmochimica Acta* 65, 2461–2467.

Du, P., Wang, S., Yuan, P., Liu, J., Liu, D., Guo, H., Xiang, X., Guo, X. (2022) Structure of allophanes with varied Si/Al molar ratios and implications to their differentiation on Mars. *Icarus* 382, 115057.

Fernandez, N.M., Zhang, X., Druhan, J.L. (2019) Silicon isotopic re-equilibration during amorphous silica precipitation and implications for isotopic signatures in geochemical proxies. *Geochimica et Cosmochimica Acta* 262, 104–127.

Frings, P.J., Clymans, W., Fontorbe, G., De La Rocha, C.L., Conley, D.J. (2016) The continental Si cycle and its impact on the ocean Si isotope budget. *Chemical Geology* 425, 12–36.

Frings, P.J., Oelze, M., Schubring, F., Frick, D.A., Blanckenburg, F. von (2021) Interpreting Silicon Isotopes in the Critical Zone. *American Journal of Science*. American Journal of Science 321.

Guertin, A. *et al.* (2024) Stable silicon isotope fractionation reflects the routing of water through a mesoscale hillslope. *Earth and Planetary Science Letters* 648, 119098.

296 Gustafsson, J.P., Lumsdon, D.G., Simonsson, M. (1998) Aluminium solubility characteristics of
297 spodic B horizons containing imogolite-type materials. *Clay Minerals* 33, 77–86.

298 Harsh, J. (2005) AMORPHOUS MATERIALS. *Encyclopedia of Soils in the Environment*.
299 Elsevier 64–71.

300 Iler, R.K. (1979) The Chemistry of Silica: Solubility, Polymerization, Colloid and Surface
301 Properties and Biochemistry of Silica. .

302 Lenhardt, K.R., Breitzke, H., Buntkowsky, G., Reimhult, E., Willinger, M., Rennert, T. (2021)
303 Synthesis of short-range ordered aluminosilicates at ambient conditions. *Scientific*
304 *Reports*. Nature Publishing Group 11, 4207.

305 Levard, C., Doelsch, E., Basile-Doelsch, I., Abidin, Z., Miche, H., Masion, A., Rose, J.,
306 Borschneck, D., Bottero, J.-Y. (2012) Structure and distribution of allophanes, imogolite
307 and proto-imogolite in volcanic soils. *Geoderma* 183–184, 100–108.

308 Nagy, K.L., Lasaga, A.C. (1993) Simultaneous precipitation kinetics of kaolinite and gibbsite at
309 80°C and pH 3. *Geochimica et Cosmochimica Acta* 57, 4329–4335.

310 Nelson, L.-A., Sanborn, P., Cade-Menun, B.J., Walker, I.J., Lian, O.B. (2021) Pedological trends
311 and implications for forest productivity in a Holocene soil chronosequence, Calvert
312 Island, British Columbia, Canada. *Canadian Journal of Soil Science*. NRC Research
313 Press 101, 654–672.

314 Oelze, M., von Blanckenburg, F., Bouchez, J., Hoellen, D., Dietzel, M. (2015) The effect of Al
315 on Si isotope fractionation investigated by silica precipitation experiments. *Chemical*
316 *Geology* 397, 94–105.

317 Ohashi, F., Wada, S.-I., Suzuki, M., Maeda, M., Tomura, S. (2002) Synthetic allophane from
318 high-concentration solutions: nanoengineering of the porous solid. *Clay Minerals* 37,
319 451–456.

320 Opfergelt, S., Delmelle, P. (2012) Silicon isotopes and continental weathering processes:
321 Assessing controls on Si transfer to the ocean. *Comptes Rendus. Géoscience* 344, 723–
322 738.

323 Opfergelt, S., Georg, R.B., Delvaux, B., Cabidoche, Y.-M., Burton, K.W., Halliday, A.N. (2012)
324 Silicon isotopes and the tracing of desilication in volcanic soil weathering sequences,
325 Guadeloupe. *Chemical Geology* 326–327, 113–122.

326 Parfitt, R.L. (2009) Allophane and imogolite: role in soil biogeochemical processes. *Clay*
327 *Minerals* 44, 135–155.

328 Rayleigh, Lord (1902) LIX. On the distillation of binary mixtures. *The London, Edinburgh, and*
329 *Dublin Philosophical Magazine and Journal of Science*. Taylor & Francis 4, 521–537.

Roerdink, D.L., van den Boorn, S.H.J.M., Geilert, S., Vroon, P.Z., van Bergen, M.J. (2015) Experimental constraints on kinetic and equilibrium silicon isotope fractionation during the formation of non-biogenic chert deposits. *Chemical Geology* 402, 40–51.

Schroeder, P.A. (ed.) (2018a) Critical Zone Clay Geochemistry. *Clays in the Critical Zone*. Cambridge University Press, Cambridge, 133–179.

Schroeder, P.A. (ed.) (2018b) What Are Clays and What Is the Critical Zone? *Clays in the Critical Zone*. Cambridge University Press, Cambridge, 1–30.

Wada, K. (1978) Chapter 4 Allophane and imogolite. *Developments in Sedimentology*. Elsevier, 147–187.

Wada, S.-I., Eto, A., Wada, K. (1979) Synthetic Allophane and Imogolite. *Journal of Soil Science* 30, 347–355.

Wang, S., Du, P., Yuan, P., Zhong, X., Liu, Y., Liu, D., Deng, L. (2018) Changes in the structure and porosity of hollow spherical allophane under alkaline conditions. *Applied Clay Science* 166, 242–249.

Ziegler, K., Chadwick, O.A., Brzezinski, M.A., Kelly, E.F. (2005) Natural variations of δ30Si ratios during progressive basalt weathering, Hawaiian Islands. *Geochimica et Cosmochimica Acta* 69, 4597–4610.

Geochemical Perspectives Letters

Rapid SRO aluminosilicate formation in a narrow pH interval fractionates silicon isotopes

K. Russo, H.T. Jamison, L.A. Derry, N.M. Fernandez

Supplementary Information

The Supplementary Information includes:

- Methods
- Statistical treatment of Figure 4 and Rayleigh Fractionation
- HAS saturation-index calculations
- Tables S-1 to S-4
- Figure S-1
- Supplementary Information References

Methods

Overview

The three experiments comprised two organosilicate-derived titrations, designated A and B, and one inorganic, amorphous silica seed or SiO_2-derived titration. Organosilicate-derived experiment A and the SiO_2-derived experiment used independent 15 mL aliquots sampled after 24 hours, whereas organosilicate-derived experiment B was titrated continuously in a 250 mL reactor and sampled after pH stabilisation. We therefore use the term *stabilised pH* when referring collectively to the three experiments.

Preparation of silicon and aluminium stock solutions

Dissolved Al stock preparation

A concentrated aluminium stock solution was prepared by dissolving anhydrous $AlCl_3$ (Thermo Scientific™, ≥ 95 %) in 1 L of ultrapure water (18.2 MΩ·cm). Dissolution of anhydrous $AlCl_3$ is strongly exothermic and generates HCl fumes, which causes evaporative mass loss during incremental addition – making gravimetric tracking of the added reagent unreliable. The final stock concentration was therefore determined by ICP-OES as 4432 ppm dissolved Al (164 mM), equivalent to the dissolution of ~ 21.9 g of $AlCl_3$. All subsequent solution preparations are reported using this measured concentration. This stock was used to generate the mixed Si –Al stock solution for both starting dissolved Si stock pathways described below.

Organosilicate-derived Si stock preparation

The organosilicate-derived Si – Al starting solutions used in titration experiments A and B were obtained from residual fluids of a precursor co-precipitation experiment conducted at 30 ºC. The parent dissolved Si stock was prepared from tetraethyl orthosilane (TEOS) following established synthesis procedures (Wada *et al.*, 1979; Ziegler *et al.*, 2005). Briefly, 30 mL of TEOS (Thermo Scientific™, 99.9%) was added to 1 L of ultrapure water and heated at 90 ºC for 5 days. After cooling to room temperature, the suspension was filtered through a 0.2 µm PES membrane (Nalgene ™ Rapid-Flow™ Sterile Disposable Filter), yielding ~ 150 ppm dissolved Si. An aliquot of the 164 mM Al stock solution (16 mL) was then added to 500 mL of the dissolved Si solution, producing nominal initial concentrations of ~ 145 ppm Si and ~ 137 ppm Al (5.2 and 5.1 mM, respectively; Si:Al ≈ 1). Parallel precursor experiments were conducted at 30 ºC, 60 ºC, and 90 ºC, but only residual fluids from the 30 ºC experiment were used in the titrations reported here.

Partial Si–Al removal occurred during the 30 ºC precursor experiment. Dissolved Si had decreased to ~ 110 ppm by the first measurement after 7 days, after which removal slowed under persistently acidic conditions (pH ≈ 3.8). After this initial decrease, dissolved Si and Al concentrations changed little with continued incubation, indicating that further precipitation had effectively stalled. This limited additional reaction is consistent with the slow rates of silica polymerisation expected under acidic conditions, where polymerisation kinetics approach a minimum (Icopini *et al.*, 2005; Iler, 1979). This behaviour motivated the controlled NaOH titration approach used to determine whether increasing alkalinity could trigger renewed Si – Al removal at room temperature.

After the precursor reactors were returned to room temperature, dissolved Si and Al concentrations decreased further and approached stable residual ranges over the following weeks. The two 30 ºC organosilicate-derived fluids subsequently used for titration contained closely similar dissolved Si concentrations of 3.24 – 3.25 mM, whereas dissolved Al ranged from 3.25 to 3.59 mM. Their initial Si/Al molar ratios therefore ranged from 0.9 to 1.0. These compositions show that substantial Si and Al remained in solution under low pH conditions, and thereby remained kinetically limited and metastable, while providing broadly comparable dissolved Si–Al inventories for the two complementary titration experiments.

Two complementary titration experiments were conducted using residual fluids from the 30 ºC precursor pathway. Organosilicate-derived experiment A used fluid collected after 28 days of preconditioning (~500 mL). The fluid was filtered three times through 0.22 µm PES membranes by vacuum filtration to remove precursor precipitates and transferred to a clean HDPE bottle. Its measured starting composition was 3.24 mM molybdate-reactive Si and 3.59 mM dissolved Al at pH 3.82, corresponding to an initial dissolved Si/Al molar ratio of 0.90. The initial dissolved δ^{30}Si was -2.64 ± 0.08 ‰. Similarly, organosilicate-derived experiment B used residual fluid from the same 30 ºC precursor pathway after 14 days of preconditioning. Its measured starting composition was 3.25 mM molybdate-reactive Si and 3.25 mM dissolved Al at pH 3.75, corresponding to an initial Si/Al molar ratio of ~ 1.0. The initial dissolved δ^{30}Si was -2.45 ± 0.15 ‰. A total of 250 mL of this fluid was subjected to vacuum filtration through 0.22 µm PES membrane, as was done for the experiment A dissolved Si stock solution to remove any potential precursor precipitates.

The organosilicate-derived starting solutions were therefore partially reacted, preconditioned Si–Al fluids rather than freshly mixed synthetic solutions. All aqueous mass balance and isotope fractionation calculations were based on the measured initial Si, Al, and δ^{30}Si composition of each experiment and its measured evolution during titration, rather than on the nominal precursor Si and Al concentrations. Saturation index calculations likewise used the measured pH, Si and Al concentration at each sampled step, supplemented by aqueous Na and Cl content reconstructed from the experimental titration history and reactor-volume corrections. Experiments A and B are treated as complementary experimental configurations as opposed to strict replicates because they differed in preconditioning duration, reactor format and sampling timescale. Nevertheless, both experiments resolve the same principal response: coupled Si–Al removal across the pH-buffering interval accompanied by progressive enrichment of the residual dissolved Si pool in ^{30}Si. The freshly prepared SiO_2-derived Si pathway provides an additional test of whether this response extends beyond the preconditioned organosilicate-derived fluids. The precursor history of these fluids, including possible sub-0.22 µm colloids or polymeric Si–Al species, remains an uncharacterized difference between the two Si source pathways.

Amorphous silica-derived Si stock preparation

The SiO_2-derived Si stock solution was prepared following methods adapted from Fernandez *et al.* (2019), Geilert *et al.* (2014), and Roerdink *et al.* (2015). Briefly, 10 g of amorphous SiO_2 (Evonik AEROSIL® OX50) was added to 1 L of ultrapure water and dissolved at 90 ºC for 7 days. The solution was cooled to room temperature and filtered (0.2 µm PES; Nalgene™ Rapid-Flow™ Sterile Disposable Filter), yielding an initially oversaturated silica solution. The filtered solution was aged for one week at room temperature, during which excess Si polymerised and settled, and was then filtered a second time at 0.2 µm. The final stock stabilised at 80 ppm (2.85 mM) molybdate-reactive Si. Like the organosilicate-derived fluid, this composition remained mildly supersaturated with respect to amorphous silica at room temperature (Gunnarsson and Arnórsson, 2000), accordant with slow silica polymerisation under mildly acidic conditions (Icopini *et al.*, 2005; Iler, 1979). A 2.97 mM (80 ppm) Al solution was prepared by dilution of the concentrated $AlCl_3$ stock. Equal volumes (250 mL each) of the Si and Al solutions were then combined, targeting ~ 1.4 mM Si and Al at a 1:1 molar ratio. Dilution upon mixing brought the combined solution below amorphous-silica saturation (Fig. S-1d). The measured starting composition was 1.28 mM Si and 1.26 mM Al, with an initial dissolved $\delta^{30}Si$ of -1.77 ± 0.05 ‰. All titration aliquots for this pathway were taken from this combined solution.

Fluid-phase sampling and analysis

Two titration configurations were used to track fluid-phase evolution during allophanic SRO HAS formation. All experiments took place in stirred reaction vessels using octagonal PTFE-coated magnetic stir bars and VWR® Advanced Magnetic Stirrers. Organosilicate-derived experiment A and the SiO_2-derived experiment were conducted as serial batch titrations using independent 15 mL aliquots. For each experiment, ~200 mL of stock solution was divided among the aliquots. One aliquot was titrated incrementally with 0.1 M NaOH (Thermo Scientific™, 99.99 %) in 0.05 – 0.1 mL increments until pH ≥ 7.0. This preliminary titration established the NaOH volumes required to bracket the initial solution, the pH-buffering interval and the post-buffering stage. Selected NaOH volumes were then added independently to the separate, fresh 15 mL aliquots, with each aliquot representing a single target point along the titration trajectory. This serial batch run approach for the titrations was adopted to satisfy the fluid volume requirements needed for subsequent geochemical analyses. The pH was measured using a Hach sensION+ MM340 benchtop meter fitted with a Sension+ 5014T combination electrode, with the standard stability criterion set to a variation of < 0.01 pH units. For each target aliquot, pH was recorded immediately after the reading stabilised (< 1 minute) and again after 24 hours. The remaining unaliquoted stock solution (~ 300 mL) from these two experiments was titrated separately to pH 7, and the resulting precipitates were recovered, washed, and dried for solid-phase characterisation.

Organosilicate-derived experiment B was conducted as a continuous titration in a single reactor containing 250 mL of starting solution. NaOH was added stepwise to the same reactor, and samples were collected after pH stabilisation following each addition, typically within 3 – 5 minutes. Three independent analytical aliquots (3 – 10 mL total sample volume) were withdrawn at each sampling step for Si isotope and dissolved-phase analyses. The measured withdrawal volume and conservative solute inventories were incorporated into the mass-balance and PHREEQC calculations (see *HAS saturation-index calculations* below). Samples from all three experiments were filtered through 0.22 µm nylon syringe filters. Filtered samples were diluted according to concentration: 20-fold below the buffering interval, 10-fold within it, and 4-fold above it. Aliquots for ICP-OES were acidified to a 2 % nitric acid (HNO_3) matrix, whereas aliquots for Si isotope and molybdate-reactive Si analyses were left unacidified.

Molybdate-reactive Si was measured for all experiments by the molybdate-blue method (Iler, 1979) on a VWR UV-1600PC spectrophotometer, with absorbance read at 660 nm against standards prepared from an Aristar® 1000 ± 8 µg/mL Si ICP standard. Dissolved Al and Si concentrations were determined by ICP-OES. Samples from the organosilicate-derived pathway were analysed at the College of Coastal Georgia on a Thermo Fisher Scientific™ iCAP PRO XP, with Al quantified on the 167.069 nm emission line (aqueous-axial-eUV mode). Samples from the SiO_2-derived pathway were analysed at Cornell University on a SPECTROBLUE, with Al and Si quantified on the 167.078 and 288.158 nm emission lines, respectively. Calibration used mixed standards prepared from Aristar® 1000 ± 8 µg/mL Si and 100 ± 0.05 µg/mL Al ICP standards. For both instruments, a 2% HNO3 wash matched the sample matrix and flushed for 60 s at 20 rpm between samples. Further, blanks were analysed every fifth sample to monitor drift. Molybdate-reactive Si was used consistently for aqueous mass balance, reaction-progress variables, Rayleigh isotope fractionation models, and PHREEQC saturation-index calculations across all three experiments. ICP-OES total

dissolved Si was additionally measured for the SiO_2-derived series and is reported in Table S-2 as an ancillary operational Si pool. Differences between total and molybdate-reactive Si provides an approximation for the amount of polymerised Si.

Silicon stable isotopes (^{28}Si, ^{29}Si, and ^{30}Si) were measured at the Institut de Physique du Globe de Paris (IPGP) on a Thermo Finnigan Neptune Plus MC-ICP-MS. Prior to analysis, samples were purified by cation-exchange chromatography (BioRad AG50W-X12 resin) to remove matrix cations, following established protocols (Georg et al., 2006; Pringle et al., 2014; van den Boorn et al., 2006). The resin was pre-cleaned with HNO3 and HCl, and Si was eluted in 5 mL of Milli-Q water to remove cationic interference. Silicon recovery yields were ~70% for the first elution step (2 mL MQ-e) with the remaining 30% obtained in the final 3 mL MQ-e step. Eluted solutions were adjusted to ~ 2 ppm Si for analysis. Samples were introduced as a wet plasma through a Standard Introduction System (SIS) with a 100 µL/min Teflon® nebulizer, and a double cyclonic spray chamber. Measurements were run at medium resolution (resolving power M/ΔM ~ 3300) to resolve the $^{30}Si - NO^+$ interference. Isotope ratios are reported in delta notation relative to the NBS-28 quartz reference standard (RM 8546) using standard-sample bracketing (López-Urzúa *et al.*, 2024):

$$\delta^{30}Si = \left[\frac{\left({}^{30}Si/{}^{28}Si \right)_{sample}}{AVG\left[\left({}^{30}Si/{}^{28}Si \right)_{std-I}, \left({}^{30}Si/{}^{28}Si \right)_{std-II} \right]} - 1 \right] \times 1000 \quad (Eq.S-1)$$

$$\delta^{29}Si = \left[\frac{\left({}^{29}Si/{}^{28}Si \right)_{sample}}{AVG\left[\left({}^{29}Si/{}^{28}Si \right)_{std-I}, \left({}^{29}Si/{}^{28}Si \right)_{std-II} \right]} - 1 \right] \times 1000 \quad (Eq.S-2)$$

where std-I and std-II are the NBS-28 standards measured immediately before and after each sample. Each sample was measured 4 times, and $\delta^{30}Si$ and $\delta^{29}Si$ are reported as the mean of these four measurements with uncertainty as 2 standard deviations (2σ). The reference materials Diatomite and BHVO-2 were analysed after every sixth sample to monitor accuracy and drift. The analysis of reference standard Diatomite (n=18) gave a $\delta^{30}Si$ value of 1.24 ± 0.01‰ while the analysis of reference standard BHVO-2 (n = 6) gave a $\delta^{30}Si$ value of -0.28 ± 0.02‰. Both reference standards agree with previous published values (Delvigne *et al.*, 2021; Jochum *et al.*, 2005; López-Urzúa *et al.*, 2024; Reynolds *et al.*, 2007). A three-isotope plot confirmed mass-dependent fractionation ($\delta^{29}Si = 0.51 \times \delta^{30}Si$) – accordingly, only $\delta^{30}Si$ is discussed in the main text.

Solid phase characterization

NaOH titration of the Si – Al solutions produce dissolved NaCl, which would contaminate the solid-phase analyses if retained. After each experiment, the supernatant was therefore repeatedly decanted and replaced with deionised water until its conductivity fell below 10 µS/cm. The washed precipitates were then dried at 30 ºC in an oven and collected for analysis. This low drying temperature was chosen deliberately because freeze-drying and higher-temperature dehydration are known to structurally modify or decompose labile SRO HAS phases (Baldermann *et al.*, 2024).

The silicon isotope composition of the SiO_2-derived precipitate was determined following the modified NaOH/alkali fusion method of (Georg *et al.*, 2006), as implemented by Fernandez *et al.* (2019, 2022) . A carefully weighed quantity of dried precipitate (20 mg) was transferred to a cleaned Ag crucible. Analytical-grade NaOH (200 mg) was added, and the sample was fused at 720 ºC for 12 minutes. The fusion product was dissolved in 15 mL ultrapure water and acidified to a 2 % HNO_3 matrix. Silicon was subsequently purified by cation-exchange chromatography (see section above *Fluid-phase sampling and analysis*) and analysed by MC-ICP-MS using the same instrumental procedure as the dissolved samples. The recovered precipitate yielded $\delta^{30}Si$ = -2.19 ± 0.11 ‰ (2σ).

X-Ray Diffraction (XRD) patterns of the washed, dried precipitates were collected at the Cornell Center for Materials Research (CCMR) on a Bruker D8 Advance ECO Powder Diffractometer (1 kW, Cu Kα = 1.5406 Å) fitted with a 160-

channel silicon strip detector. Patterns were acquired from 5 to 90º 2θ at a step size of 0.015º2θ per step and 0.100 s per step. Samples were mounted as powder on a zero-background Si holder.

Scanning electron microscopy (SEM) imagery was performed on a JEOL JSM-IT700HR SEM under high vacuum in secondary-electron mode at 10.0 kV (instrument probe-current setting 50.0). Powder samples were mounted on a double-sided carbon tape and carbon-coated using a (Cressington) 108 Manual Sputter Coater with an MTM-10 thickness monitor. Coat thicknesses were 42.4 nm (organosilicate-derived A) and 58.8 nm (SiO_2-derived). Elemental distribution maps were acquired with an SEM-mounted Oxford Instruments Ultim Max 100 EDS detector. EDS mapping was used qualitatively, to assess the spatial co-location of Si and Al in the precipitates. No matrix-matched standards were employed, and no quantitative compositions are reported from EDS.

Fourier-transform infrared (FTIR) spectra were collected for both precipitates, using different configurations at the two host institutions. The organosilicate-derived precipitate was analysed by an Attenuated Total Reflectance (ATR) at the College of Coastal Georgia on a ThermoScientific™ Nicolet iS5 spectrometer with an iD7 monolithic diamond ATR accessory. The reported spectrum represents the co-addition of 16 scans at 2 cm^{-1} resolution (0.964 cm^{-1} data spacing), with background corrections completed hourly. The SiO_2-derived precipitate was analysed in transmission at the CCMR on a Bruker Vertex 80v vacuum-bench spectrophotometer over 4000 – 400 cm^{-1} at 4 cm^{-1} resolution. For transmission analysis, the sample was first dried at 60 ºC for 24 hours to reduce adsorbed moisture while preserving structural hydroxyl groups. Approximately 3 mg of finely ground powder was mixed with 300 mg of spectroscopic-grade KBr (Thermo Scientific™; 1: 100 w/w), homogenised by hand crushing in an agate mortar, and pressed uniaxially at 10 t for 3 minutes under vacuum to yield optically translucent pellets. Because ATR and transmission measurements can differ slightly in apparent band positions and relative intensities, spectral comparisons between the two precipitates (**Fig. 3a**) are based on the broad diagnostic absorption envelopes of SRO HAS rather than on exact band positions.

Statistical treatment of Figure 4 and Rayleigh Fractionation

Reduced major axis regression for dissolved δ^{30}Si versus f_{Al}

Reduced major axis (RMA) regressions were used to describe the relationship between dissolved δ^{30}Si and the fraction of Al remaining in solution (f_{Al}) **in Fig. 4a**. To achieve our goal to describe the bivariate relationship between Al removal and Si isotope fractionation, RMA regression was favoured over that of ordinary least squares (OLS) because both variables contain analytical or propagated experimental uncertainty. This uncertainty in both dimensions fails to satisfy the implicit error-free, independent variable condition in OLS regression to predict dissolved δ^{30}Si (y) from f_{Al} (x). This follows standard guidance for Model II regression approaches, which are commonly used when both variables are subject to uncertainty or when the fitted line is intended to describe the relationship between two measured quantities (McArdle, 2003; Warton *et al.*, 2006).

For each experiment, the RMA slope was calculated as:

$$b_{\mathrm{RMA}} = \mathrm{sign}(r)\frac{s_y}{s_x} \quad (Eq. S-3)$$

where r is the Pearson correlation coefficient, and s_y and s_x are the sample standard deviations of dissolved δ^{30}Si and f_{Al}, respectively. The intercept is then calculated as:

$$a_{\mathrm{RMA}} = \bar{y} - b_{\mathrm{RMA}}\bar{x} \quad (Eq. S-4)$$

Reported R^2 values are squared Pearson correlation coefficients (r^2), following common reporting practice for RMA regressions, and are used here as descriptive measures of bivariate association as opposed to the OLS residual-based coefficients of determination (Warton *et al.*, 2006, 2012).

RMA regression parameters for all three experiments are summarised in Table S-3. The organosilicate-derived regressions, based on 12 (experiment A) and 9 (experiment B) isotope measurements, both yielded strong negative associations between dissolved δ^{30}Si and f_{Al} (Pearson r = -0.998 and -0.952, respectively). Their slopes differ (-2.04 and -1.41), which may reflect differences in preconditioning history, reactor configuration, and sampling timescale that distinguish these complementary experiments. The SiO_2-derived regression was based only on 3 isotope measurements and is included as strictly a descriptive trend; its slope and R^2 are treated qualitatively (Table S-3, footnote A).

Rayleigh fractionation model

Rayleigh distillation models were used to describe the Si stable isotope evolution of the residual dissolved Si pool during progressive Si removal (**Fig. 4b**). Rayleigh fractionation is a conventional stable isotope framework for systems in which a finite, well-mixed reactant pool is progressively converted into a product that is removed from further reaction, such that the isotopic composition of the residual reactant evolves as a function of the fraction of reactant remaining (Rayleigh, 1902). Such models have been frequently implemented to interpret δ^{30}Si fractionation both in laboratory and field studies (Fernandez *et al.*, 2019; Frings *et al.*, 2016; Georg *et al.*, 2007; Hughes *et al.*, 2013; Opfergelt and Delmelle, 2012). In this study, the Rayleigh model was found to be an appropriate first-order description of the observed dissolved δ^{30}Si because both experiments displayed progressive dissolved Si removal and subsequent enrichment of the residual fluid pool in ^{30}Si. This behaviour is generally described as kinetic isotope fractionation and is driven by the formation of solid precipitates from solution, which preferentially incorporates lighter ^{28}Si, leaving the residual solution δ^{30}Si to shift towards higher values (Frings *et al.*, 2016; Ziegler *et al.*, 2005). The magnitude of the fractionation is quantified by the fractionation factor (α or ε [‰], Eq. S-5), and the direction is interpreted as consistent with kinetic isotope fractionation when $\alpha < 1$ or $\varepsilon < 0$ ‰.

In a Rayleigh treatment, the residual dissolved reactant described by the following expression:

$$\delta^{30}\mathrm{Si}_{\mathrm{fluid}} = (1000 + \delta^{30}\mathrm{Si}_0) f_{\mathrm{Si}}^{(\alpha-1)} - 1000 \quad (Eq.S-5)$$

here $\delta^{30}\mathrm{Si}_0$ is the measured initial dissolved Si isotope composition for each starting Si solution pathway, f_{Si} is the fraction of dissolved Si remaining in solution, and α is the fitted fractionation factor. The corresponding per mil description for the size of the isotopic fractionation (ε) can be defined as:

$$\varepsilon\,[‰] \approx 1000 \times ln\alpha \quad (Eq.S-6)$$

The accumulated reaction product can similarly be described with the expression:

$$\delta^{30}\mathrm{Si}_{\mathrm{accum}} = (1000 + \delta^{30}\mathrm{Si}_0)\left(\frac{1 - f_{\mathrm{Si}}^{\alpha}}{1 - f_{\mathrm{Si}}}\right) - 1000 \quad (Eq.S-7)$$

The accumulated product curve predicted by the Rayleigh model represents the integrated isotopic composition of the total Si removed from solution up to each value of f_{Si}. It is therefore distinct from the instantaneous product composition, which would represent the δ^{30}Si of material forming at a specific reaction step (Frings *et al.*, 2016).

Rayleigh fits were performed separately for a given experiment by weighted nonlinear least squares. For each fit, the measured initial dissolved δ^{30}Si was set as $\delta^{30}\mathrm{Si}_0$, f_{Si} was used as the independent variable, and the fractionation factor (α) was treated as the sole fitted parameter. The reported 2σ analytical uncertainty on dissolved δ^{30}Si was used to weight the fit. Model performance was evaluated using RMSE (Root Mean Square Error) and reduced χ^2, which were used as our primary fit-quality metrics because they describe residual magnitude and uncertainty-weighted misfit, respectively.

The resulting best-fit α was converted to ε via Eq. (S-6), which serves to quantify pathway-specific apparent isotope effects during net Si removal associated with SRO HAS formation. We explicitly define the Rayleigh-derived ε as an "apparent" rather than an "intrinsic" kinetic fractionation factor. An intrinsic kinetic ε would require Si removal to be definitively irreversible over the timescale of the experiment. However, SRO HAS precipitation is a reversible mineral-

fluid reaction. As such, a limited back-reaction or surface exchange yielding partial Si isotopic re-equilibration (Fernandez *et al.*, 2019; Roerdink *et al.*, 2015; Stamm *et al.*, 2019) cannot be completely ruled out – even if this effect is minimal in the experimental duration of our study. The best fit ε values therefore represent apparent net fractionation parameters and describes the net isotope effect recorded by the residual Si pool during Si removal. This interpretation follows the use of Rayleigh models as endmember descriptions in Si isotope studies, while recognizing that δ^{30}Si signatures during secondary silicate formation can evolve away from simple irreversible Rayleigh behaviour when back-reaction or re-equilibration becomes important (Fernandez *et al.*, 2019).

HAS saturation-index calculations

Saturation indices (SI = log (IAP/K_{sp})) were calculated for the three titration experiments at each sampled reaction step using PHREEQC v3 and the minteq.v4 thermodynamic database (Parkhurst and Appelo, 2013). Aqueous concentrations from Tables S-1 and S-2 were used for PHREEQC. Dissolved Al values reported below the 0.02 mM analytical detection limit were assigned to 0.01 mM, corresponding to half the detection limit, for the purpose of these calculations.

The minteq.v4 database was chosen for consistency within the solubility framework developed by Baldermann *et al.*(2024) who similarly used the same aqueous activity model to constrain the composition-dependent solubility of SRO HAS phases. Allophanic SRO HAS is not included as a standard database phase and, thus, a separate custom HAS phase was defined for each experiment using the ion activity product and composition-solubility relationship reported by Baldermann *et al.*(2024) (their Eq. 5; pK_{HAS} = log K_{sp}).

$$IAP = \frac{\left(Al^{3+}_{(aq)}\right)^2 \cdot \left(H_4SiO_{4(aq)}\right)^x}{\left(H^{+}_{(aq)}\right)^6} \quad (Eq.S-8)$$

$$x = 2 \cdot \left(\frac{Si}{Al}\right)_{solid} \quad (Eq.S-9)$$

and the reported linear regression between pK_{HAS} and the Si/Al of the precipitate (Eq. 7 in Baldermann *et al.*, 2024)) follows as,

$$pK_{HAS} = 2.9 \cdot \left(\frac{Al}{Si}\right)_{solid} + 7.9 \quad (Eq.S-10).$$

The precipitate compositions were estimated from cumulative aqueous mass balance using the $(Si/Al)_{removed}$ relationship defined in Equation 1 of the main text. For organosilicate-derived Si experiment A and the SiO_2-derived Si experiment, the ratios were evaluated at the end of their principal coupled-removal intervals at pH 4.88 and 4.79, respectively. For organosilicate-derived experiment Si B, the final pH 6.03 point was used because substantial Al removal continued between pH 4.72 and the final sample, where dissolved Al had decreased below the analytical detection limit (Table S-1). The resulting $(Si/Al)_{removed}$ values of 0.52, 0.49, and 0.47 for organosilicate-derived Si experiments A and B and the SiO_2-derived Si experiment, respectively, correspond to estimated $(Al/Si)_{solid}$ of 1.92, 2.04, and 2.13. These yield experiment-specific HAS solubility constants (pK_{HAS}) of ~13.5, 13.8, and 14.1 following the Baldermann et al. (2024) relationship. The latter two $(Al/Si)_{solid}$ estimates lie slightly beyond the upper end of the composition range used to calibrate the regression ($(Al/Si)_{solid}$ = 1.3 – 2.0; Su and Harsh, 1998) and are therefore treated as a minor extrapolation.

Each experiment-specific phase was added to the PHREEQC input using the balanced reaction:

$$Al_2O_3(SiO_2)_{x\,(s)} \cdot 3H_2O + 6H^{+}_{(aq)} \rightleftharpoons xH_4SiO_{4(aq)} + (6 - 2x)H_2O \quad (Eq.S-11)$$

The aqueous inputs were measured stabilised pH, 0.22-µm filtered molybdate-reactive Si, and dissolved Al at 20 ºC. Dissolved Na was calculated from the cumulative amount of NaOH added, whereas dissolved Cl was calculated from the initial $AlCl_3$ inventory. For the independent-aliquot experiments, dissolved Na and Cl were corrected for dilution by the added titrant. For the continuous organosilicate-derived Si B experiment, reactor volume and conservative dissolved Na and Cl inventories were updated recursively after each NaOH addition and after removal of the three independently

collected analytical aliquots. Because the tabulated Si and Al concentrations for experiment B had been corrected to remove titrant dilution effects they were converted back to the concentrations present in the reactor at each sampled step before PHREEQC aqueous speciation calculations.

The resulting aqueous activities of Al^{3+} and H_4SiO_4 were used to calculate saturation indices for the corresponding experiment-specific SRO HAS phase. The same modelled solutions were then evaluated with respect to three other candidate phases: amorphous $Al(OH)_3$ (log K_{sp} = 10.8 from WATEQF; Hem and Roberson, 1967), gibbsite (log K_{sp} = 8.11, Palmer and Wesolowski, 1992; Wesolowski, 1992) and amorphous silica (log K_{sp} = -2.714; Gunnarsson and Arnórsson, 2000). All calculated activities and saturation indices are reported in Table S-4.

All three experiments became strongly oversaturated with respect to their experiment-specific allophanic SRO HAS phases across the pH-buffered, Si –Al removal intervals (Fig. S-1a). Within the shaded intervals, SI_{HAS} ranged from +3.27 to +4.46 for organosilicate-derived Si experiment A, +1.80 to +4.07 for organosilicate-derived Si experiment B, and +2.27 to +2.77 for the SiO_2-derived Si experiment. Experiment B began close to the estimated HAS equilibrium at pH 3.75 (SI_{HAS} = + 0.12), but became increasingly oversaturated as alkalinity was added, reaching SI_{HAS} = +5.20 at the final pH 6.03 point. These values indicate a strong thermodynamic driving force for SRO HAS precipitation as the fluids passed through the pH-buffering interval.

In contrast, all three experiments remained undersaturated with respect to amorphous $Al(OH)_3$ during their principal coupled-removal intervals (Fig. S-1b). Over these intervals, $SI_{amAl(OH)_3}$ ranged from -1.46 to -0.70 in organosilicate-derived experiment A, -2.10 to -0.85 in organosilicate-derived experiment B, and -1.58 to -1.27 in the SiO_2-derived experiment. A discrete amorphous Al-hydroxide phase was therefore predicted to be thermodynamically unfavourable during the interval in which the majority of Al removal and dissolved $\delta^{30}Si$ evolution occurred.

Gibbsite was nominally supersaturated throughout much of the titration series (Fig. S-1c). Within the active removal intervals, $SI_{gibbsite}$ ranged from +1.10 to +1.86, +0.46 to +1.70 and +0.97 to +1.28 for organosilicate-derived Si A, organosilicate-derived Si B, and the SiO_2-derived Si experiment, respectively. Supersaturation alone does not necessarily demonstrate that gibbsite precipitated, particularly over the reaction timescales of these experiments (minutes to hours) at around room temperature. Under these conditions, poorly ordered Al-bearing precursor phases are expected to form more readily than crystalline Al hydroxides (Hem and Roberson, 1967), coherent with kinetic inhibition and the Ostwald step rule (Steefel and Van Cappellen, 1990). The amorphous $Al(OH)_3$ endmember therefore provides the more relevant thermodynamic constraint on whether a discrete Al-hydroxide phase could account for the observed rapid Al removal.

The amorphous-silica saturation states differed between the two dissolved Si source pathways (Fig. S-1d). The SiO_2-derived Si solution remained undersaturated with respect to amorphous silica throughout the titration, with $SI_{SiO_{2(am)}}$ ranging from -0.14 to -0.48. Its substantial Si removal therefore cannot be explained by precipitation of a discrete amorphous silica phase. Both organosilicate-derived Si solutions started mildly supersaturated with respect to amorphous silica. During the high removal intervals, $SI_{SiO_{2(am)}}$ ranged from +0.25 to -0.07 in experiment A and from +0.26 to +0.04 in experiment B. Experiment A crossed into undersaturation between 4.61 and 4.88, whereas experiment B became undersaturated by the final pH 6.03 point ($SI_{SiO_{2(am)}}$= -0.06). Minor silica polymerisation cannot therefore be excluded during the early organosilicate-derived titration steps. However, Si removal continued as the fluids approached or crossed amorphous silica equilibrium, while Al was removed concurrently and the solutions remained substantially more oversaturated with respect to the experiment-specific SRO HAS phases.

Taken together, the saturation index calculations are most consistent with formation of an Al-rich, SRO HAS-dominated precipitate during the pH-buffered reaction interval. They argue against amorphous $Al(OH)_3$ as a significant independent Al sink and exclude discrete amorphous silica as the principal Si sink in the freshly prepared SiO_2-derived Si experiment. Reported $Al(OH)_{3(s)}$ solubility constants span log Ks ≈ 8 – 11 with increasing crystallinity (Nordstrom and May, 1995). Our conclusion that a discrete Al-hydroxide phase was not a significant additional Al sink holds for any constant in the upper (amorphous) part of this range. Minor silica polymerisation cannot be definitively excluded in the organosilicate-

derived fluids, but the combined aqueous and solid-phase evidence indicates that SRO HAS was the dominant reaction product.

Supplementary Tables

Table S-1 Results of Organosilicate-derived Si titration

I.D.	0.1 M NaOH (mL)	pH t=0	pH *stabilized*	Dissolved Reactive Si mM ± (1σ)	Dissolved Al mM ± (1σ)	Dissolved $\delta^{29}Si$ ‰ ± (2σ)	Dissolved $\delta^{30}Si$ ‰ ± (2σ)
A-0	0	3.83	3.82	3.24 ± 0.01	3.59 ± 0.01	-1.33 ± 0.03	-2.64 ± 0.08
A-1	0.1	4.13	4.14	3.13 ± 0.01	3.37 ± 0.01	-1.25 ± 0.04	-2.52 ± 0.05
A-2	0.2	4.21	4.07	3.13 ± 0.01	3.44 ± 0.01	-1.31 ± 0.02	-2.60 ± 0.04
A-3	0.3	4.27	4.06	3.11 ± 0.01	3.38 ± 0.01	-1.31 ± 0.03	-2.60 ± 0.07
A-4	0.55	4.39	4.07	3.12 ± 0.01	3.37 ± 0.01	-1.27 ± 0.03	-2.56 ± 0.05
A-5	0.8	4.45	4.25	3.09 ± 0.01	3.46 ± 0.01	-1.32 ± 0.05	-2.56 ± 0.10
A-6	0.9	4.52	4.36	2.66 ± 0.01	2.34 ± 0.02		
A-7	1.05	4.68	4.51	2.12 ± 0.01	1.42 ± 0.02	-0.75 ± 0.06	-1.51 ± 0.06
A-8	1.1	4.74	4.61	1.87 ± 0.01	1.01 ± 0.04	-0.62 ± 0.03	-1.28 ± 0.06
A-9	1.15	4.93	4.88	1.50 ± 0.01	0.25 ± 0.02	-0.31 ± 0.04	-0.63 ± 0.09
A-10	1.2	5.59	5.26	1.33 ± 0.01	< 0.02	-0.29 ± 0.06	-0.67 ± 0.10
A-11	1.25	6.11	5.71	1.21 ± 0.01	< 0.02	-0.31 ± 0.02	-0.68 ± 0.03
A-12	1.3	6.75	6.78	1.06 ± 0.01	< 0.02	-0.36 ± 0.05	-0.66 ± 0.14
B-0	0	-	3.75	3.25 ± 0.06	3.25 ± 0.02	-1.12 ± 0.07	-2.45 ± 0.15
B-1	2	-	4.04	3.25 ± 0.11	3.06 ± 0.01	-1.09 ± 0.07	-2.42 ± 0.11
B-2	4	-	4.16	3.15 ± 0.06	2.82 ± 0.01	-1.09 ± 0.05	-2.39 ± 0.04
B-3	6	-	4.23	3.06 ± 0.06	2.65 ± 0.02	-1.03 ± 0.05	-2.24 ± 0.10
B-4	8	-	4.28	3.03 ± 0.01	2.45 ± 0.04	-1.00 ± 0.07	-2.21 ± 0.04
B-5	12	-	4.34	2.92 ± 0.01	1.98 ± 0.01	-0.98 ± 0.07	-2.15 ± 0.04
B-6	16	-	4.54	2.40 ± 0.02	1.02 ± 0.01	-0.84 ± 0.10	-1.83 ± 0.06
B-7	18	-	4.72	2.08 ± 0.02	0.51 ± 0.01	-0.65 ± 0.05	-1.57 ± 0.11
B-8	20	-	6.03	1.67 ± 0.01	< 0.02	-0.34 ± 0.02	-0.90 ± 0.09

Table S-2 Results of SiO_2-derived Si titration

I.D.	0.1 M NaOH (mL)	pH t=0	pH *stabilized*	Dissolved Reactive Si[A] mM ± (1σ)	Dissolved Total Si[B] mM ± (1σ)	Dissolved Al mM ± (1σ)	δ^{29}Si Fluid ‰ ± (2σ)	δ^{30}Si Fluid ‰ ± (2σ)
0	0	4.01	4.01	1.28 ± 0.02	1.40 ± 0.01	1.26 ± 0.01	-1.00 ± 0.09	-1.77 ± 0.05
1	0.05	4.28	4.28	1.25 ± 0.01	1.45 ± 0.02	1.07 ± 0.01	-	-
2	0.1	4.32	4.29	1.24 ± 0.01	1.28 ± 0.02	1.20 ± 0.01	-	-
3	0.15	4.4	4.33	1.22 ± 0.01	1.48 ± 0.02	1.13 ± 0.01	-	-
4	0.2	4.42	4.32	1.19 ± 0.01	1.22 ± 0.02	1.16 ± 0.01	-	-
5	0.25	4.46	4.33	1.24 ± 0.04	1.42 ± 0.04	1.21 ± 0.01	-	-
6	0.3	4.47	4.33	1.18 ± 0.01	1.57 ± 0.01	1.14 ± 0.02	-	-
7	0.35	4.49	4.38	1.13 ± 0.01	1.35 ± 0.01	0.99 ± 0.01	-	-
8	0.4	4.5	4.4	1.05 ± 0.01	1.43 ± 0.01	0.66 ± 0.15	-	-
9	0.45	4.61	4.45	0.97 ± 0.01	1.17 ± 0.01	0.64 ± 0.01	-0.82 ± 0.20	1.51 ± 0.06
10	0.5	4.72	4.67	0.91 ± 0.01	1.21 ± 0.01	0.18 ± 0.01	-	-
11	0.55	4.91	4.79	0.72 ± 0.01	0.78 ± 0.02	0.06 ± 0.02	-	-
12	0.6	5.46	5.95	0.58 ± 0.01	0.62 ± 0.01	< 0.02	-	-
13	0.65	8.12	8	0.62 ± 0.01	0.62 ± 0.01	0.03 ± 0.01	-0.67 ± 0.10	-1.23 ± 0.13

A. Molybdate-reactive Si concentration measured with UV-Vis spectroscopy
B. Total dissolved Si measured by ICP-OES

Table S-3 Statistical summary for Figure 4 RMA regressions and Rayleigh model fits

Parameters	Organosilicate-derived Si A	Organosilicate-derived Si B	SiO_2-derived Si[A]
Dissolved δ^{30}Si vs. f_{Al} regression statistics			
n	12	9	3
RMA slope	-2.039	-1.408	-0.553
RMA slope 95% CI	-2.130*(low)* – -1.942*(high)*	-1.842*(low)* – -1.076*(high)*	NA
RMA intercept	-0.634	-1.163	-1.221
Pearson *r*	-0.998	-0.952	-0.9997
R^2	0.996	0.907	0.999
Rayleigh model fit statistics			
$\delta^{30}Si_0$	-2.64	-2.45	-1.77
α	0.99743 *(0.99792)*[B]	0.9978	0.9992
SE(α)	7×10^{-5} *(3×10^{-5})*	0.0001	0.0001
ε (‰)	-2.56 *(-2.08)*	-2.20	-0.80
SE (ε) (‰)	0.07 *(0.03)*	0.13	0.14
RMSE (‰)	0.04 *(0.19)*	0.06	0.04
Reduced χ^2	0.54 *(6.27)*	0.38	0.22

A. The SiO_2-derived Rayleigh and RMA parameters are descriptive fits through 3 measurements and are, thus, only treated qualitatively.
B. Italicized values correspond to the Rayleigh-derived values obtained from considering the full trajectory (*i.e.* all data) whereas non-italicized values correspond to those obtained by considering only data that falls within the Al-coupled Si removal interval.

Table S-4 Summary of PHREEQC-calculated saturation indices for Si pathway-specific SRO HAS phases, amorphous Al-hydroxide ($Al(OH)_3$), gibbsite, and amorphous silica at 20 ºC.

Exp.	$\log a_{Al^{3+}}$	$\log a_{H_4SiO_4}$	SI_{HAS}	$SI_{Al(OH)_3}$	$SI_{gibbsite}$	$SI_{SiO_{2(am)}}$
Organosilicate-derived starting dissolved Si						
A-0	-3.0291	-2.4867	0.8027	-2.7013	-0.1457	0.2654
A-1	-3.0589	-2.5018	2.6475	-1.771	0.7846	0.2503
A-2	-3.0529	-2.5018	2.2396	-1.975	0.5806	0.2504
A-3	-3.0603	-2.5045	2.1618	-2.0125	0.5431	0.2476
A-4	-3.068	-2.5031	2.2079	-1.9902	0.5654	0.2491
A-5	-3.0745	-2.5072	3.2705	-1.4568	1.0989	0.2451
A-6	-3.2077	-2.5727	3.5960	-1.2599	1.2957	0.1795
A-7	-3.4013	-2.6717	4.0057	-1.0035	1.5521	0.0805
A-8	-3.5471	-2.7264	4.2571	-0.8493	1.7063	0.0258
A-9	-4.2041	-2.8224	4.4632	-0.6962	1.8594	-0.0703
A-10	-5.8824	-2.8748	3.332	-1.2346	1.3211	-0.1226
A-11	-6.5352	-2.9158	4.6836	-0.5374	2.0182	-0.1637
A-12	-9.2026	-2.9736	5.7086	0.0052	2.5608	-0.2215
B-0	-3.0569	-2.4855	0.1192	-2.9390	-0.3834	0.2666
B-1	-3.0864	-2.4891	1.7966	-2.0985	0.4571	0.2630
B-2	-3.1223	-2.5063	2.4279	-1.7745	0.7811	0.2458
B-3	-3.1516	-2.5225	2.7735	-1.5938	0.9619	0.2296
B-4	-3.1862	-2.5304	2.9965	-1.4784	1.0772	0.2217
B-5	-3.2746	-2.5538	3.1569	-1.3868	1.1688	0.1984
B-6	-3.5566	-2.6465	3.7023	-1.0688	1.4868	0.1057
B-7	-3.8805	-2.7125	4.0701	-0.8527	1.7029	0.0397
B-8	-7.1990	-2.8119	5.1961	-0.2412	2.3144	-0.0597
SiO_2 - derived starting dissolved Si						
0	-3.2795	-2.8919	0.6874	-2.3813	0.1743	-0.1400
1	-3.3541	-2.9023	2.1486	-1.6459	0.9097	-0.1503
2	-3.3195	-2.9057	2.2746	-1.5813	0.9743	-0.1537
3	-3.3467	-2.9128	2.4535	-1.4885	1.0671	-0.1608
4	-3.3398	-2.9236	2.3972	-1.5117	1.0440	-0.1716
5	-3.3294	-2.9056	2.4947	-1.4713	1.0843	-0.1537
6	-3.3526	-2.9272	2.4281	-1.4945	1.0611	-0.1752
7	-3.4102	-2.946	2.5954	-1.4021	1.1535	-0.1941
8	-3.5637	-2.9781	2.3785	-1.4956	1.0601	-0.2261
9	-3.5858	-3.0125	2.6021	-1.3677	1.1879	-0.2605
10	-4.1491	-3.0404	2.7695	-1.271	1.2846	-0.2884
11	-4.6651	-3.1421	2.3626	-1.4269	1.1287	-0.3902
12	-6.9744	-3.2361	4.6162	-0.2563	2.2993	-0.4841
13	-13.3578	-3.2129	4.1711	-0.4897	2.0659	-0.4609

Supplementary Figures

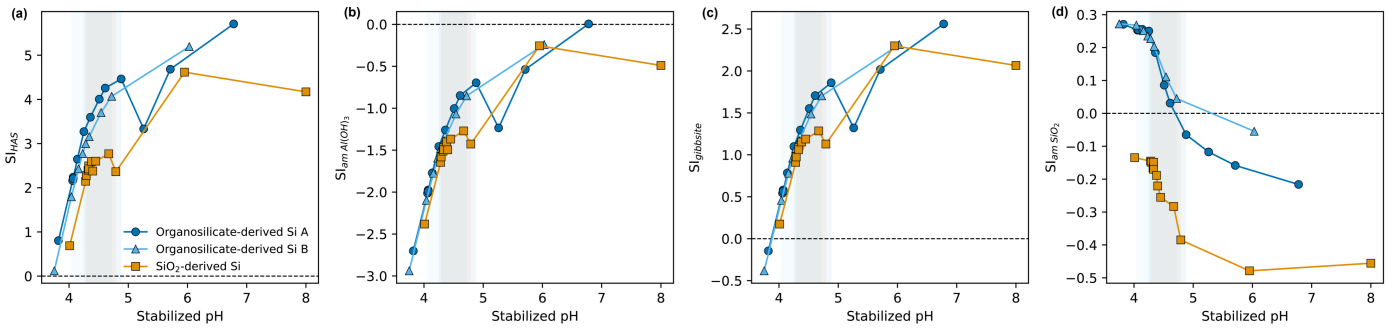

Figure S-1 Saturation indices (SI) for the reactive solutions with respect to **(a)** experiment-specific allophanic SRO HAS (SI_{HAS}), **(b)** amorphous $Al(OH)_3$ ($SI_{amAl(OH)_3}$), **(c)** gibbsite ($SI_{gibbsite}$), and **(d)** amorphous SiO_2 ($SI_{am\,SiO_2}$) plotted against stabilised pH for all three titration experiments. Organosilicate-derived Si experiment A and the SiO_2-derived Si experiment were sampled after 24 hours, whereas organosilicate-derived experiment B was titrated continuously and sampled after pH stabilisation (typically within 30 – 45 minutes, *Methods*). Shaded bands mark the main Si – Al removal intervals defined in the main text: pH 4.25 – 4.88 for organosilicate-derived Si A, pH 4.04 – 4.72 for organosilicate-derived Si B, and pH 4.29 – 4.79 for the SiO_2-derived Si experiment. Dashed lines mark equilibrium (SI = 0). Calculations were performed in PHREEQC using the minteq.v4 database at 20 ºC (Parkhurst and Appelo, 2013), with experiment-specific HAS phases defined using the composition-dependent solubility framework of Baldermann *et al.* (2024). Solubility constants for the reference phases are from Hem and Roberson (1967) (amorphous $Al(OH)_3$), Palmer and Wesolowski (1992) (gibbsite), and Gunnarsson and Arnórsson (2000) (amorphous SiO_2). All three experiments were strongly oversaturated with respect to SRO HAS across the removal intervals, while remaining undersaturated with respect to amorphous $Al(OH)_3$. The SiO_2-derived Si solution remained undersaturated with respect to amorphous silica throughout, whereas the organosilicate-derived solutions evolved from mild supersaturation toward or below equilibrium as Si–Al removal progressed.

Supplementary Information References

Baldermann, A., Stamm, F.M., Farkaš, J., Löhr, S., Ratz, B., Letofsky-Papst, I., Dietzel, M. (2024) Precipitation of short-range order hydroxy aluminosilicate (HAS) and hydrous ferric silicate (HFS) at ambient temperature: Insights into mineral formation pathways, crystal chemistry and solubility-stability relationships. *Chemical Geology* 646, 121911.

Delvigne, C. *et al.* (2021) Silicon Isotope Analyses of Soil and Plant Reference Materials: An Inter-Comparison of Seven Laboratories. *Geostandards and Geoanalytical Research* 45, 525–538.

Fernandez, N.M., Bouchez, J., Derry, L.A., Chorover, J., Gaillardet, J., Giesbrecht, I., Fries, D., Druhan, J.L. (2022) Resiliency of Silica Export Signatures When Low Order Streams Are Subject to Storm Events. *Journal of Geophysical Research: Biogeosciences* 127, e2021JG006660.

Fernandez, N.M., Zhang, X., Druhan, J.L. (2019) Silicon isotopic re-equilibration during amorphous silica precipitation and implications for isotopic signatures in geochemical proxies. *Geochimica et Cosmochimica Acta* 262, 104–127.

Frings, P.J., Clymans, W., Fontorbe, G., De La Rocha, C.L., Conley, D.J. (2016) The continental Si cycle and its impact on the ocean Si isotope budget. *Chemical Geology* 425, 12–36.

Geilert, S., Vroon, P.Z., Roerdink, D.L., Van Cappellen, P., van Bergen, M.J. (2014) Silicon isotope fractionation during abiotic silica precipitation at low temperatures: Inferences from flow-through experiments. *Geochimica et Cosmochimica Acta* 142, 95–114.

Georg, R.B., Reynolds, B.C., Frank, M., Halliday, A.N. (2006) New sample preparation techniques for the determination of Si isotopic compositions using MC-ICPMS. *Chemical Geology* 235, 95–104.

Georg, R.B., Reynolds, B.C., West, A.J., Burton, K.W., Halliday, A.N. (2007) Silicon isotope variations accompanying basalt weathering in Iceland. *Earth and Planetary Science Letters* 261, 476–490.

Gunnarsson, I., Arnórsson, S. (2000) Amorphous silica solubility and the thermodynamic properties of H4SiO°4 in the range of 0° to 350°C at Psat. *Geochimica et Cosmochimica Acta* 64, 2295–2307.

Hem, J.D., Roberson, C.E. (1967) Form and stability of aluminium hydroxide complexes in dilute solution. *Geol. Surv. Water-Supply Pap. (U.S.); (United States)* 1827-A.

Hughes, H.J., Sondag, F., Santos, R.V., André, L., Cardinal, D. (2013) The riverine silicon isotope composition of the Amazon Basin. *Geochimica et Cosmochimica Acta* 121, 637–651.

Icopini, G.A., Brantley, S.L., Heaney, P.J. (2005) Kinetics of silica oligomerization and nanocolloid formation as a function of pH and ionic strength at 25°C. *Geochimica et Cosmochimica Acta* 69, 293–303.

Iler, R.K. (1979) The Chemistry of Silica: Solubility, Polymerization, Colloid and Surface Properties and Biochemistry of Silica. .

Jochum, K.P., Nohl, U., Herwig, K., Lammel, E., Stoll, B., Hofmann, A.W. (2005) GeoReM: A New Geochemical Database for Reference Materials and Isotopic Standards. *Geostandards and Geoanalytical Research* 29, 333–338.

López-Urzúa, S., Luu, T.-H., Derry, L. (2024) Assessment of matrix effects induced by chloride, sulfate and dissolved organic carbon during Si isotope measurements by MC-ICP-MS under wet plasma conditions. *Journal of Analytical Atomic Spectrometry* 39, 1033–1042.

McArdle, B.H. (2003) Lines, models, and errors: Regression in the field. *Limnology and Oceanography* 48, 1363–1366.

Nordstrom, D.K., May, H.M. (1995) Aqueous Equilibrium Data for Mononuclear Aluminum Species. *The Environmental Chemistry of Aluminum*. CRC Press.

Opfergelt, S., Delmelle, P. (2012) Silicon isotopes and continental weathering processes: Assessing controls on Si transfer to the ocean. *Comptes Rendus. Géoscience* 344, 723–738.

Palmer, D.A., Wesolowski, D.J. (1992) Aluminum speciation and equilibria in aqueous solution: II. The solubility of gibbsite in acidic sodium chloride solutions from 30 to 70°C. *Geochimica et Cosmochimica Acta* 56, 1093–1111.

Parkhurst, D.L., Appelo, C. a. J. (2013) *Description of input and examples for PHREEQC version 3: A computer program for speciation, batch-reaction, one-dimensional transport, and inverse geochemical calculations*. *Techniques and Methods*. U.S. Geological Survey.

Rayleigh, Lord (1902) LIX. On the distillation of binary mixtures. *The London, Edinburgh, and Dublin Philosophical Magazine and Journal of Science*. Taylor & Francis 4, 521–537.

Reynolds, B.C. *et al.* (2007) An inter-laboratory comparison of Si isotope reference materials. *Journal of Analytical Atomic Spectrometry* 22, 561–568.

Roerdink, D.L., van den Boorn, S.H.J.M., Geilert, S., Vroon, P.Z., van Bergen, M.J. (2015) Experimental constraints on kinetic and equilibrium silicon isotope fractionation during the formation of non-biogenic chert deposits. *Chemical Geology* 402, 40–51.

Stamm, F.M., Zambardi, T., Chmeleff, J., Schott, J., von Blanckenburg, F., Oelkers, E.H. (2019) The experimental determination of equilibrium Si isotope fractionation factors among H4SiO4o, H3SiO4− and amorphous silica (SiO2·0.32 H2O) at 25 and 75 °C using the three-isotope method. *Geochimica et Cosmochimica Acta* 255, 49–68.

Steefel, C.I., Van Cappellen, P. (1990) A new kinetic approach to modeling water-rock interaction: The role of nucleation, precursors, and Ostwald ripening. *Geochimica et Cosmochimica Acta* 54, 2657–2677.

Su, C., Harsh, J.B. (1998) DISSOLUTION OF ALLOPHANE AS A THERMODYNAMICALLY UNSTABLE SOLID IN THE PRESENCE OF BOEHMITE AT ELEVATED TEMPERATURES AND EQUILIBRIUM VAPOR PRESSURES. *Soil Science* 163, 299.

Wada, S.-I., Eto, A., Wada, K. (1979) Synthetic Allophane and Imogolite. *Journal of Soil Science* 30, 347–355.

Warton, D.I., Duursma, R.A., Falster, D.S., Taskinen, S. (2012) smatr 3– an R package for estimation and inference about allometric lines. *Methods in Ecology and Evolution* 3, 257–259.

Warton, D.I., Wright, I.J., Falster, D.S., Westoby, M. (2006) Bivariate line-fitting methods for allometry. *Biological Reviews* 81, 259–291.

Wesolowski, D.J. (1992) Aluminum speciation and equilibria in aqueous solution: I. The solubility of gibbsite in the system Na-K-Cl-OH-Al(OH)4 from 0 to 100°C. *Geochimica et Cosmochimica Acta* 56, 1065–1091.

Ziegler, K., Chadwick, O.A., Brzezinski, M.A., Kelly, E.F. (2005) Natural variations of δ30Si ratios during progressive basalt weathering, Hawaiian Islands. *Geochimica et Cosmochimica Acta* 69, 4597–4610.